Impact of Minimal Silver Incorporation on Chalcopyrite Absorbers—Origins for Improved Open-Circuit Voltages in (Ag,Cu)(In,Ga)Se_2 Solar Cells

Sateesh Prathapani, Sevan Gharabeiki, Jakob Lauche, René Schwiddessen, Pablo Reyes-Figueroa, Nikolaus Weinberger, Michele Melchiorre, Rutger Schlatmann, Iver Lauermann, and Christian Alexander Kaufmann*

The influence of minimal amounts of Ag (0.5–1.4 at%) on elemental distribution and crystalline quality of (Ag,Cu)(In,Ga)Se_2 (ACIGSe) absorbers grown by the three-stage coevaporation without added alkali elements is reported. The elemental ratios affect the amount of Ag to be uniformly incorporated into the chalcopyrite absorber and the open-circuit voltage (V_{OC}) of the ACIGSe solar cell devices. Ag-containing absorbers deposited at 530 °C achieve a best photoconversion efficiency of 18.2%. Due to an increased V_{OC}, ACIGSe absorbers perform better than their Ag-free variants at low deposition temperatures. The factors contributing to this increased V_{OC} of low-temperature devices are: 1) enhanced elemental Ga and In interdiffusion and hence their spatial distribution across the absorber thickness, leading to an increase in the minimum bandgap, 2) an improved absorber crystalline quality with larger grains resulting in high quasi-Fermi-level splitting and lower nonradiative losses. The photoluminescence data obtained on the ACIGSe absorbers reveal the corresponding variations in their bandgap and photoluminescence quantum yield. These material-level insights into Ag incorporation in chalcopyrite help to advance the development of chalcopyrite-based tandem solar cells, which—so far—is limited by the requirement of high deposition temperatures.

1. Introduction

Several researchers have recently demonstrated low-bandgap Cu(In,Ga)Se_2 (CIGSe) photovoltaic (PV) solar cells as bottom cells incorporated in perovskite–CIGSe tandems and InGaP/GaAs//CIGSe triple-junction devices with high power conversion efficiencies (PCEs) of 29.9% and 30%, respectively.[1–4] These novel combinations demonstrate that the CIGSe thin-film PV technologies can be employed as highly efficient bottom cells that yield high efficiencies, which can be targeted for space applications requiring flexibility and light weight.[5–7] Conventionally, the CIGSe solar absorbers are deposited at high temperatures, typically at 530–600 °C onto standard float glass, high-temperature stable glass, or steel substrates in either rigid or flexible form.[8,9] High growth temperatures ensure the formation of the desired chalcopyrite crystal structure, minimizing the presence of impurity phases. However, lowering the CIGSe deposition temperature adds versatility in adapting low-melting-point substrates such as flexible polyimide.[10] Adding silver (Ag) to CIGSe makes it possible to realize efficient low-temperature growth, forming ACIGSe ((Ag,Cu)(In,Ga)Se_2).[10–13] Being isoelectronic, Ag acts to substitute Cu partially. The presence of Ag in CIGSe lowers the melting point, enhances grain growth, reduces the density of detrimental defects in the absorber bulk, and improves the carrier lifetime.[10–14] Additionally, it is critical to comprehend how Ag affects CIGSe at the materialistic level in order for it to display such beneficial materials properties. An understanding initially developed for low-bandgap ACIGSe can then be extended to wide-bandgap, Se-based chalcopyrite compositions, which are anticipated to be used as top cell devices in tandem solar cells.[15,16] In view of possible new

S. Prathapani, J. Lauche, R. Schwiddessen, P. Reyes-Figueroa, R. Schlatmann, I. Lauermann, C. A. Kaufmann
Helmholtz-Zentrum Berlin für Materialien und Energie GmbH (HZB)
Hahn-Meitner-Platz 1, 14109 Berlin, Germany
E-mail: sateesh.prathapani@gmail.com

The ORCID identification number(s) for the author(s) of this article can be found under https://doi.org/10.1002/solr.202400863.

DOI: 10.1002/solr.202400863

S. Gharabeiki, M. Melchiorre
Department of Physics and Materials Science
University of Luxembourg
4422 Belvaux, Luxembourg

N. Weinberger
Thin Layer Technology Unit
Department of Structural Engineering and Material Sciences
Universität Innsbruck
6020 Innsbruck, Austria

tandem solar cell combinations with CIGSe, we conduct this study on low-bandgap ACIGSe grown at different temperatures adding minimal amounts of Ag to determine the changes that occur at the material level.

Depending on the (Ga/In) ratios, the bandgap (E_g) of CIGSe varies in the range 1.04–1.68 eV.[17] Ag incorporation was demonstrated in CIGSe of different bandgaps.[10,12,18,19] For ACIGSe with a bandgap of 1.15 eV, maintaining AAC ([Ag]/([Ag] + [Cu])) at 19%, a PCE of 23.64% was reported. These ACIGSe absorbers were deposited at 530 °C.[20] With an AAC at 4.7%, about 20.1% PCE was achieved for ACIGSe of 1.12 eV bandgap, where these ACIGSe absorbers were grown at a relatively low temperature of 450 °C.[11] Further, the low-temperature growth of ACIGSe made it possible to realize a PCE of 19.77% for bifacial CIGSe solar cells.[21] However, for innovative next-generation CIGSe-based tandem/multijunction solar cells, ACIGSe of relatively low bandgap ($\leq$1.1 eV) is desirable in order to use them as efficient bottom cells.[6] It was reported that Ag addition increases the absorber bandgap.[18] Hence, it is our interest to know the extent of the possible bandgap increase for a given amount of Ag addition, even when it is added in minimal quantity. There is a debate about how much Ag is favorable for a particular CIGSe composition considering a miscibility gap of Ag in CIGSe, which depends on the ACIGSe growth temperatures and Ga content.[22,23] From an economic perspective, use of a noble metal such as Ag adds costs. Considering these factors, it is logical to find out the minimum amount of Ag required to achieve the advantageous effects for a particular deposition condition.

Typically, CIGSe solar absorbers of Cu-poor composition are used to fabricate high-PCE devices. The Cu-poor characteristic of a CIGSe absorber is defined by its CGI ratio ([Cu]/([Ga] + [In])) being less than 1. Though near-stoichiometric Cu-rich CIGSe absorbers (with CGI close to one) possess superior material properties, on the contrary, the Cu-deficient (CGI < 1) compositions are found to yield high PCE when used in solar cells.[24] The PCE loss observed for Cu-rich compositions is attributed to the higher carrier recombination losses at the absorber/buffer layer (and/or) buffer layer/window layer interfaces compared to Cu-poor compositions.[24–26] In Cu-poor CIGSe, the recombination is dominant in the bulk of the absorber.[24] It is therefore imperative to evaluate the optimal CGI or ACGI ([Ag] + [Cu])/([Ga] + [In]) values of ACIGSe absorbers to yield the best PCE.

In this article, we develop an understanding of ACIGSe absorbers deposited at various temperatures with varying Ag contents and the corresponding material property changes. We focus on the ACIGSe compositions with only minimal incorporation of Ag, namely, AAC% of 0%, 2%, 3%, and 6%, aiming to produce absorbers of low bandgaps around 1.1 eV or below. These low AAC% represent a very low atomic concentration (at%) of Ag in these absorbers around 0.5, 0.7, and 1.4 at%, respectively, for AAC% of 0%, 2%, 3%, and 6%. We used the physical vapor deposition (PVD) method to coevaporate Cu, In, Ga, and Se onto a Ag precursor layer in three stages to form ACIGSe absorbers as described in the Experimental Section. The absorbers were produced at three different deposition temperatures 530, 450, and 370 °C to assess the Ag influence on the absorber crystalline quality and elemental distributions. For each absorber deposition temperature, we evaluate, 1) how a certain degree of Cu deficiency (i.e., CGI) influences the Ag distribution and its impact on the elemental interdiffusion, characterized by glow discharge optical emission spectrometry (GDOES) profiles, 2) how the presence of Ag influences the absorber crystallization and causes the secondary phases to appear, characterized by grazing-incidence X-ray diffraction (GIXRD), and 3) how Ag influences the resulting absorber bandgap and the nonradiative (NR) losses by recording absolute photoluminescence (PL) and photoluminescence quantum yield (PLQY), respectively. With these results in connection with the devices' PCE, we elucidate the influence of Ag on the open-circuit voltage (V_{OC}) and further demonstrate that a minimum quantity of AAC, 2% (0.5 at%), can effectively increase it. In this study, the usual practice of alkali postdeposition treatments commonly followed in the state-of-the-art CIGSe absorber fabrication processes is intentionally avoided to solely investigate the influence of Ag.[27] This study involves only pure Se-based CIGSe or ACIGSe compositions.

2. Results and Discussion

2.1. ACIGSe Thin-Film Solar Absorber Growth

We employ the Ag–metal precursor layer approach for ACIGSe deposition. The Ag-precursor layer was deposited by sputtering onto the Mo-coated soda lime glass (SLG) substrates. The Ag-precursor layer thickness was calculated based on the required Ag molar ratio in ACIGSe for a given absorber thickness. About 10, 15, and 30 nm thin Ag-precursor layers were used. The 10 nm Ag-precursor layer thickness is the minimum reproducible limit in our sputter system. To form ACIGSe, the Ag-coated Mo/SLG substrates (Ag/Mo/SLG) were inserted into the PVD chamber, and then elemental Cu, In, and Ga were coevaporated in different stages under a Se-rich environment. **Figure 1** shows the schematic of our typical three-stage coevaporation process. Stage-1 comprises two steps in which elemental Ga (stage-1a) and In (stage-1b) were supplied sequentially. In stage-2, elemental Cu was supplied until the resulting composition reached an end point beyond the first stoichiometric point (SP1), where ACGI > 1. This detection is possible for our PVD processes by in situ monitoring of the substrate heater power and also through laser light scattering.[28] At the end of stage-2, the absorbers were rich in Cu for Ag-free compositions or rich in (Ag + Cu) for Ag-containing compositions. In stage-3, Ga and In were supplied simultaneously to achieve CGI < 1 (for Ag-free compositions) or ACGI < 1 (for Ag-containing compositions), resulting in final group [I] poor compositions after crossing the second stoichiometric point (SP2). Between stage-2 and stage-3 there is an intermediate annealing step maintaining the same stage-2 deposition temperature for 3 min. In all three stages, Se was continuously supplied throughout the duration of the deposition. The substrate temperature for all the depositions during stage-1 was 300 °C, and in stages 2 and 3, it was varied for different depositions as 530, 450, and 370 °C. For a fair comparison, the absorbers with different AAC% were grown in the same deposition runs. After deposition, the absorbers were characterized for elemental analysis using X-ray fluorescence (XRF), as determined at% of various elements are given in the Table ST1, Supporting Information.

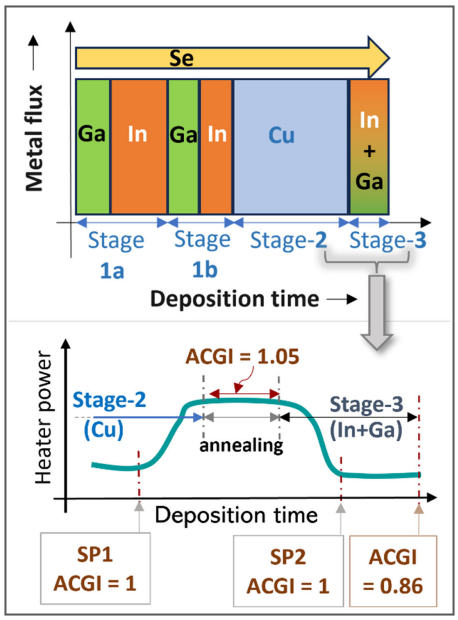

Figure 1. Schematic representation of ACIGSe solar absorber growth in a three-stage PVD deposition process. The schematic also provides the information on identifying SP1, SP2, and ACGI values with the markings made on the heater power profile at different stages of the deposition.

2.2. Device Performance Dependency on CGI and ACGI

The elements of ACIGSe are from groups I–III–VI (where, I: Cu, Ag, III: Ga, In, and VI: Se). For a fixed CGI composition, Ag addition (appears as AAC) increases the net group [I] content, that is, increases the ACGI value. **Figure 2**a–d, displays PCE, open-circuit voltage (V_{OC}), short-circuit current density (J_{SC}), and fill factor (FF) dependencies on CGI and AAC for the various ACIGSe devices, respectively. The standard active area of these devices is around 0.91 cm^2 fully produced at HZB and Table ST2, Supporting Information, provides the performance parameters. Among these ACIGSe devices of PVD@530, 450, and 370 °C with different AAC, absorbers with AAC 2–3% yielded either a competing or an enhanced performance compared to Ag-free compositions processed at their respective PVD temperatures. Especially for low-temperature devices (≤450 °C), increased V_{OC} is the main reason for the improved PCE within AAC 2–3%. To support this observation, current–voltage curves obtained on the devices of AAC 0% and 2% are shown in Figure 2e and their external quantum efficiency (EQE) plots are shown in Figure S1, Supporting Information. In this set, devices of PVD@450 °C with AAC 2% outperform even the high-temperature PVD@530 °C devices yielding a best PCE of 16.5%. This proves that Ag addition into CIGSe is effective for the absorbers produced at relatively low temperatures. On increasing the Ag content further to AAC 6%, no further PCE improvement is observed for the devices of these three different PVD temperatures. From Table ST2, Supporting Information, it is evident that for AAC 2–3% the absorber's ACGI is found to be in the range of 0.86–0.88 corresponding to a CGI range of 0.84–0.86. For relatively higher Ag content, where AAC is 6%, the absorber's ACGI values exceed this favorable range, resulting in PCE loss. Alternatively, maintaining ACGI of 0.87 (which is the favorable range in previous case), absorbers grown with a combination of low CGI (0.81) and high AAC (6%) at PVD@530 °C resulted in a loss in V_{OC}, affecting the PCE again (Figure 2f). Furthermore, the low CGI of 0.81 even for the Ag-free compositions resulted in V_{OC} loss making it clear that there is an inherent challenge with highly Cu-poor (i.e., CGI < 0.84) absorbers not capable of producing high V_{OC}. Thus, we can state that maintaining a sufficient CGI (i.e., 0.84–0.86) is beneficial in achieving higher V_{OC}.

To further confirm the favorable limit of ACGI with a combination of sufficient CGI (i.e., 0.84–0.86) and low AAC (2–3%), a second set of ACIGSe absorbers were fabricated at HZB and complete devices were produced in a different laboratory at University of Luxembourg (LU) depositing similar buffer layer, window layer, and metal contacts and subsequently PCE measurements were carried out there. Figure S2, Supporting Information, presents the summary of performance parameters from the respective current–voltage curves drawn on these devices of active areas 0.43–0.49 cm^2. Among these devices, again absorbers containing Ag with ACGI of 0.86–0.88 and AAC of 2% achieved better results, which are in good agreement with the earlier fully produced device results with 0.91 cm^2 standard active areas at HZB (Table ST2, Supporting Information). In this set of small active area devices, which were completed at LU, a highest PCE of 18.2% (J_{SC}: 36.8 mA cm^{-2}, V_{OC}: 0.656 V, FF: 0.75) for AAC 2% (i.e., ACGI 0.86–0.88) (for absorbers of PVD@530 °C) was observed (Figure S2e, Supporting Information). In summary, we can state that among as-prepared ACIGSe absorbers of different PVD temperatures, a CGI range of 0.84–0.86 with AAC 2% that results in ACGI of 0.86–0.88 yielded the best device PCE with improved V_{OC}. However, a lower CGI or higher ACGI that is out of this specified range resulted in V_{OC} loss.

2.3. Ag Distribution Based on CGI and ACGI

Figure 3a and S3, Supporting Information, show the GDOES data plots of Cu and Ag in-depth distributions in ACIGSe absorbers of different AAC, for which the deposition was stopped at the end of stage-2 (referred to as "stage-2 ACIGSe"). These absorbers were fabricated using two different stage-2 growth temperatures, that is, 530 °C (Figure 3a) and 450 °C (Figure S3, Supporting Information). It is evident from these two figures that at the end of stage-2, where ACGI ≈0.99–1.03, irrespective of the Ag content present in the absorber, Ag depletes from the absorber bulk and concentrates at the surface. Predominantly, Cu shows a uniform distribution across the bulk of the absorber at stage-2. For AAC 6%, a high concentration of Ag at the surface partially depletes the Cu. These preferential elemental distributions at the end of stage-2 reveal the nature of the group [I] elements in ACIGSe, establishing the fact that even though the Ag was added to the growing absorber as a precursor layer, when Cu surplus prevails, Ag exhibits high diffusivity in the chalcopyrite structure and reaches the absorber surface depleting from the bulk. At the end of stage-2, the Cu is preferentially accommodated in the bulk of the absorber, replacing the Ag.

The ACIGSe samples from the complete stage-3 process with a final CGI 0.86 have shown a uniform Ag distribution for AAC

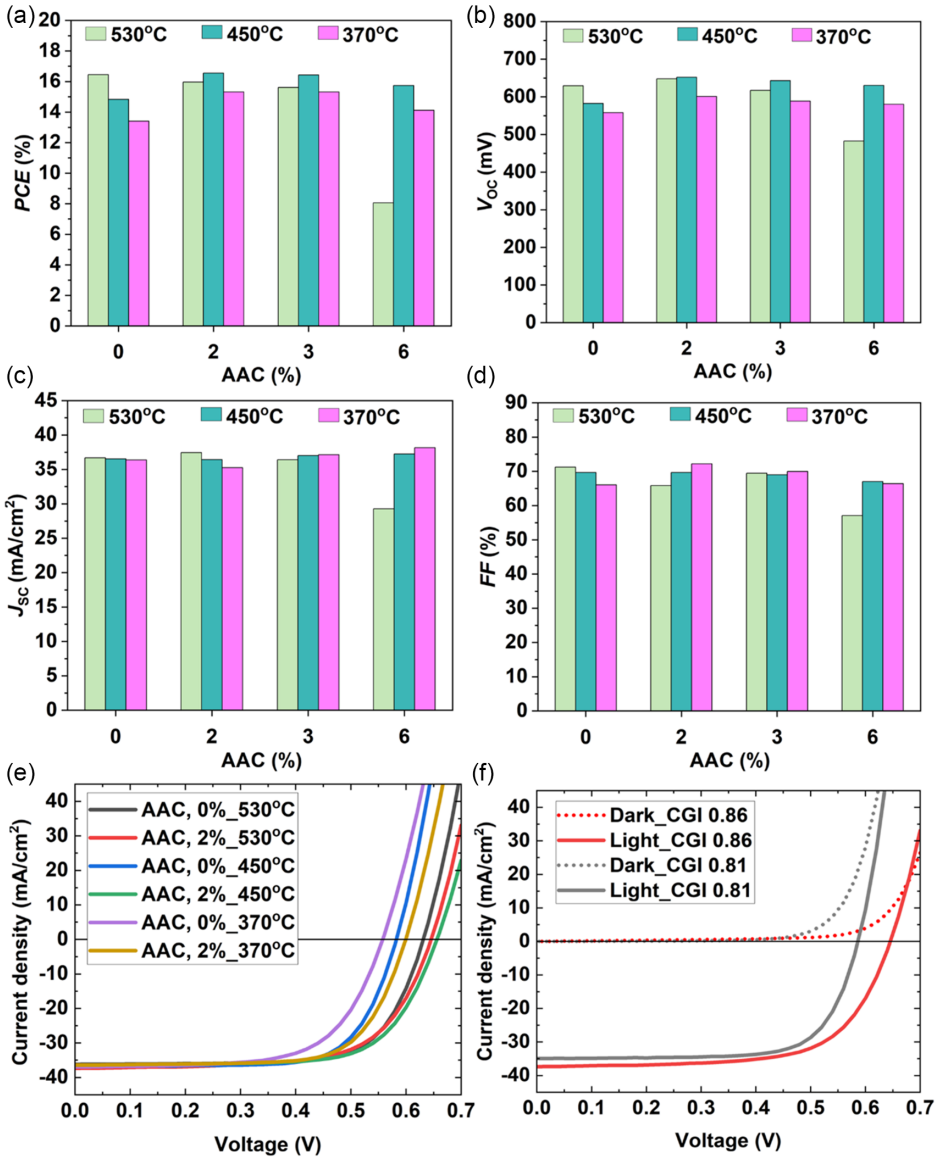

Figure 2. a–d) The best solar cell performance parameters of ACIGSe devices (whose absorber's CGI range is 0.84–0.86) extracted from their current–voltage scans and plotted against AAC% with respect to PVD process temperatures (fully produced at HZB with cell active area 0.91 cm^2), e) current–voltage scans of ACIGSe devices with AAC 0% and 2% at different absorber's PVD temperatures (CGI range 0.84–0.86), and f) current–voltage scans of PVD@530 °C ACIGSe devices with two different absorber's CGI and AAC combinations (CGI 0.81, AAC 6% and CGI 0.86, AAC 2%) that have their ACGI in the same range.

2–3% (Figure 3b) with ACGI of around 0.88, and these are the absorbers that showed high V_{OC} in this study. For these stage-3 absorbers with the CGI of 0.86, maintaining AAC 6%, again the Ag concentration at the absorber surface appears (Figure 3b) (Ag distribution profile is not flat), which could be due to the increased ACGI beyond the favorable limit that restricts the Ag to diffuse into the bulk uniformly. To investigate the dependency of the Ag distribution on CGI further, let us consider the GDOES plots recorded on stage-3 ACIGSe absorbers of low CGI, that is, CGI of 0.81 (Figure 3c). It is clear from Figure 3c that with lower CGI of 0.81 there is a relatively better Ag distribution across the bulk of the absorber with flatter Ag distribution profiles even for AAC 6%. Therefore, a lower CGI leads to a more pronounced Ag distribution incorporating higher amounts of Ag uniformly across the absorber. However, being low in CGI even with improved Ag distribution, these absorbers did not yield high V_{OC} (as earlier shown in Figure 2f). Though it is interesting to carry out a detailed study revealing the origins of the voltage losses for highly Cu-poor (CGI < 0.84) ACIGSe that are high in Ag, it is beyond the scope of the current manuscript.

To summarize the observation on overall Ag distribution and associated CGI dependency on the device results, we can state that for the absorbers produced by our three-stage deposition method, a high deficiency of Cu (CGI of 0.81) drives high amounts of Ag (AAC 6%) uniformly into the absorber bulk; however, a favorable overall absorber's CGI (0.84–0.86) with

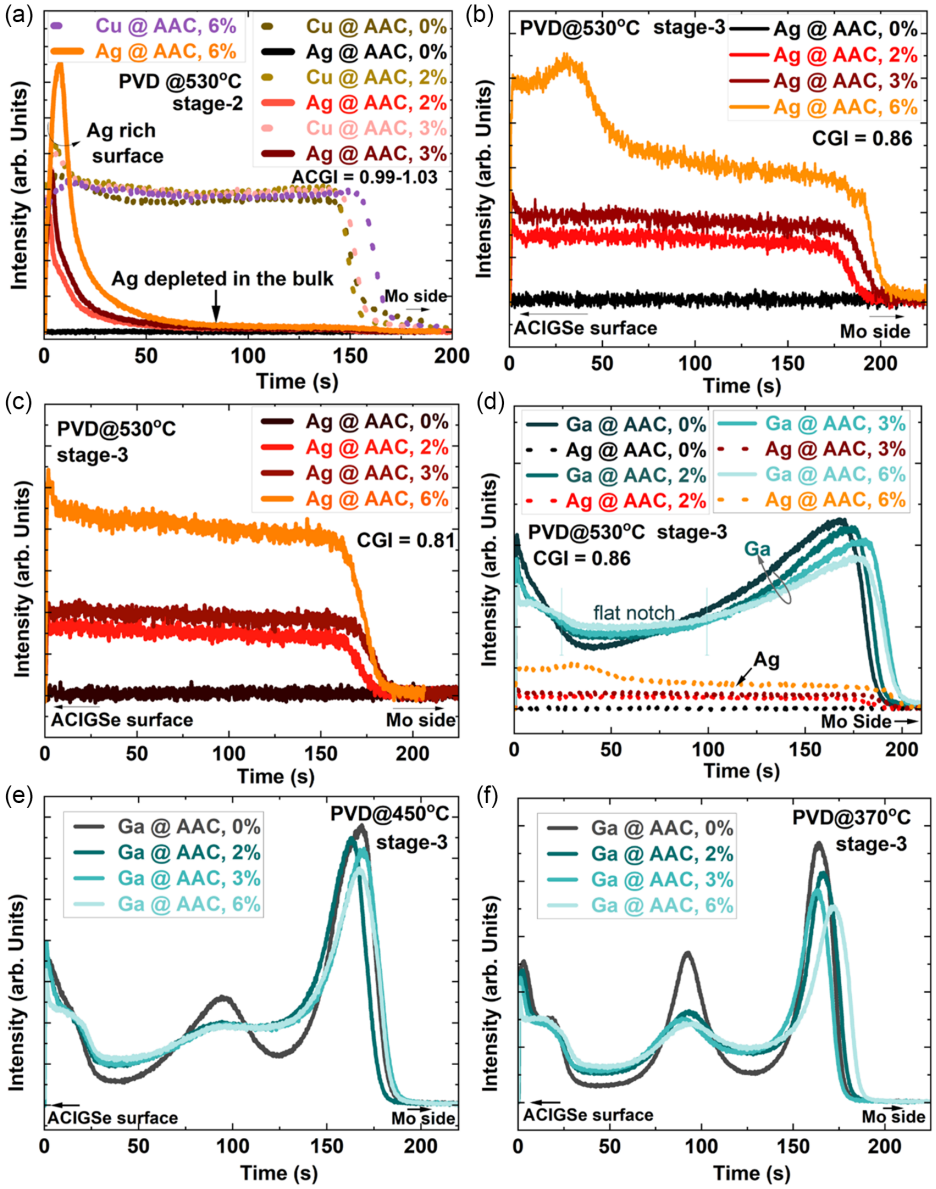

Figure 3. GDOES depth profiles on ACIGSe absorbers, a) at the end of stage-2 deposited at a temperature of 530 °C with ACGI = 0.99–1.03, b) at the end of stage-3, deposited at a temperature of 530 °C with CGI = 0.86, c) at the end of stage-3, deposited at a temperature of 530 °C with CGI, 0.81, and d–f) influence of Ag on Ga distribution at the end of stage-3 for the absorbers deposited at a PVD temperature of 530, 450, and 370 °C, respectively.

AAC (2–3%) resulting in an ACGI of (0.86–0.88) yielded high V_{OC}. To re-emphasize, these observations are made on the absorbers that did not receive any intentional alkali treatments.

2.4. Influence of Ag-Induced Elemental Distribution on the ACIGSe Bandgap

We observed that the deposition temperatures and the amount of Ag influence the interdiffusion and the distribution of Ga and In. At high temperature (530 °C), enhanced elemental diffusion allows Ga and In to distribute evenly, resulting in smoother GDOES profiles, as shown in (Figure 3d and S4a, Supporting Information). At low deposition temperatures, insufficient thermal energy inhibits Ga and In interdiffusion, leading to less uniform elemental distributions, as shown in (Figure 3e,f and S4b,c, Supporting Information). These GDOES profiles for low-temperature absorbers reveal concentrated regions of Ga and In corresponding to their deposition sequence; however, the presence of Ag improves their interdiffusion to some extent altering their distribution in those concentrated regions. Typically, our standard CIGSe absorbers are produced with a V-shape Ga grading to reduce carrier losses at the front and back interfaces; thus, a notch region appears in the GDOES Ga profiles.[11,29] With the incorporation of Ag, this notch region (Ga profile) gets flatter with its surrounding region becoming less steep.

In CIGSe chalcopyrite absorbers, the bandgap depends on the composition and therefore on the elemental distribution of Ga and In across the absorber. If the absorbers are grown with a compositional notch region low in Ga or rich in In, the minimum bandgap reduces, whereas, if this notch region is rich in Ga or low in In, the minimum bandgap widens. For all the absorbers containing Ag, there is an increased Ga content (Figure 3d–f) at the notch region irrespective of the shape of its profile. Therefore, a higher bandgap could be expected for ACIGSe of all AAC% compared to Ag-free compositions. Additionally, with the incorporation of Ag, the steepness of the Ga profile reduces on both sides of this notch region, which signifies the variation in the extent of bandgap increase around this notch region among these ACIGSe samples. With these observations from GDOES, it is convincing to state that the increase in the bandgap of these ACIGSe absorbers of AAC 2, 3, and 6% could have origins predominantly from increased Ga content at this notch region and cannot be solely attributed as an inherent Ag contribution disrupting the band structure. We present the determined bandgap values using PL measurements recorded on these ACIGSe absorbers in **Table 1**, which displays higher-bandgap values for Ag-containing absorbers.

2.5. Influence of Ag on Absorber Crystallization and Microstructure

We elucidate here the influence of Ag on the ACIGSe crystallization and phase purity at various depths from the film surface by recording GIXRD patterns on ACIGSe absorbers, which were collected at the end of stage-2 and stage-3. Information on GIXRD angles and probing depths is given in the supporting information. To simplify the discussion, we selected appropriate samples for this crystallization discussion that best represents the Ag influence. For samples of stage-2, ACIGSe absorbers are selected from the PVD@450 °C process, and for stage-3, absorbers are selected from the processes of all three PVD temperatures under consideration.

From **Figure 4**a, the diffractograms of stage-2 (PVD@450 °C) absorbers with AAC 6% show all the characteristic peaks of the polycrystalline chalcopyrite phase for all grazing angles, that is, throughout the probed depth of around 1.4 μm from the absorber surface, these diffractograms show a dominant 112-peak. It is well known that a Cu-rich growth at the end of stage-2 forms a conductive β-CuSe secondary phase and this phase is reported to create detrimental shunt paths causing carrier recombination in CIGSe devices.[30,31] Our Ag-free absorbers of stage-2 (Figure 4b) show the presence of β-CuSe.[32] We identified a β-CuAgSe secondary phase in the stage-2 Ag-rich (ACGI > 1) ACIGSe absorbers coexisting with the chalcopyrite primary phase.[33] The secondary-phase peaks are dominant at the absorber surface (Figure 4a_GIXRD@0.25°) and their intensity reduces toward its bulk (Figure 4a_higher grazing angles) which correspond to an Ag distribution observed through GDOES profiles as shown earlier in Figure 2a. The GIXRD results obtained on lower Ag content, that is, AAC 2% and 3%, also showed the presence of a β-CuAgSe impurity phase (Figure 4b) after stage-2 group [I]-rich growth (where ACGI > 1). This crystallographic information reveals the nature of Ag in ACIGSe chalcopyrite: even with its minimal quantity, Ag has less tendency to be a part of the bulk chalcopyrite system and prefers to precipitate out as β-CuAgSe for group [I]-rich absorber growth. During the stage-3, these group [I]-rich ACIGSe absorbers were exposed to Ga and In with a constant Se-background. As a result, their effective CGI lowers, which could be a favorable condition for β-CuAgSe to dissolve, thus allowing Ag to diffuse into the absorber bulk and be incorporated into the chalcopyrite phase during stage-3 ACIGSe recrystallization. Structurally, Ag incorporation was successfully found in chalcopyrite form with no apparent traces of a β-CuAgSe impurity phase after stage-3 for all CGI of 0.81–0.86 considered here and also for ACGI up to 0.92 (Figure S5a, Supporting Information). A shift in the 112-peaks of the surface diffractograms of ACIGSe (Figure S5b, Supporting Information) indicates a change in the interplanar spacing due to a variation in the Ag-induced elemental interdiffusion for a given deposition temperature.

From the diffractograms, the line broadening of hkl reflections measured using integral breadth reveals the information on crystallite size and strain.[34] Here, we define the crystalline quality using the integral breadths (β_{hkl}) as a quantitative parameter that qualitatively assesses both size and strain effects. The ACIGSe absorbers considered in the study possess a variety of compositional gradients across the absorber thickness. It is complex to present a quantitative comparative study on lattice constants, crystallite size, and strain to determine the crystalline quality against the Ag content and PVD growth temperatures used. However, introducing a simple method of determining and comparing the integral breadth (β_{112}) values of the 112-peak from the GIXRD diffractograms of various ACIGSe absorbers can assess the crystalline quality. A poor crystalline quality due to a smaller crystallite size or microstrain or their combination results in an increased β_{112}. Also, a local compositional gradient

Table 1. The parameters obtained from absolute PL measurements on different absorbers which are used for ACIGSe device voltage loss analysis presented in Figure 6.

PVD [°C]	AAC [%]	($E_{g\text{-}PL}$)[a] [eV]	$\left(V_{OC}^{SQ}\right)_{PL}$ [mV]	PLQY	Average NR-loss [meV] (k_BT ln(PLQY))[a]	QFLS [meV]	Interface losses [mV] (QFLS/q − V_{OC})	Device V_{OC} (Avg.)[a] [mV]
530	0	1.06	823.7	9.46×10^{-4}	177.5	646.2	13.9	632.3
530	2	1.11	870.7	3.86×10^{-4}	200.6	670.1	23.4	646.7
450	0	1.02	786.1	1.51×10^{-4}	224.5	561.6	5.2	556.4
450	2	1.05	814.5	4.51×10^{-4}	196.4	618.1	12.5	605.6

[a]Error: $E_{g\text{-}PL}$ (±5–6 meV), NR losses (±7 meV), V_{OC} (±1.5–8.0 mV).

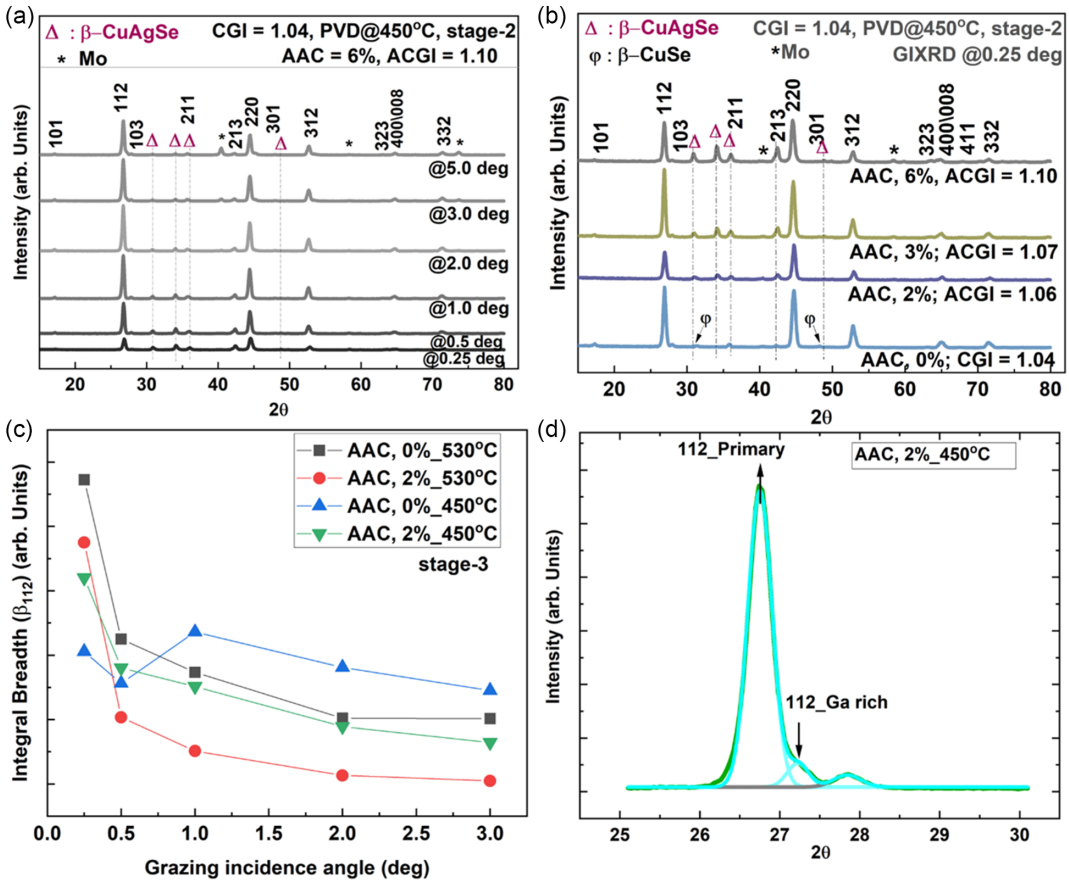

Figure 4. a,b) GIXRD diffractograms recorded on stage-2 ACIGSe samples deposited at 450 °C having ACGI > 1, (a) β-CuAgSe secondary-phase peaks appear for AAC 6%, (b) the absorber Ag-rich surfaces show β-CuAgSe peaks for AAC, 2%, 3% along with AAC 6%, and the β-CuSe impurity phase for Ag-free composition, and c) integral breadth (β_{112}) variation with respect to grazing-incident angles for ACIGSe of AAC, 0%, and 2% deposited each at two different PVD temperatures 530 and 450 °C, d) GIXRD of 5° incidence angle recorded on stage-3 ACIGSe samples deposited at 450 °C showing two distinguishable characteristic 112 peaks in the absorber bulk that correspond to chalcopyrite of primary phase (112_primary) and a chalcopyrite of secondary phase (112_Ga rich), respectively.

can establish a variation in the local lattice parameters resulting in an increased peak broadening (i.e., increased β_{112}).[35] The compositional gradients in chalcopyrite absorbers could cause structural defects.[36] Irrespective of a particular structural imperfection, an increase in the magnitude of β_{112} qualitatively establishes the poor crystalline quality of the absorber. Therefore, β_{112} obtained from GIXRD diffractograms referring to various depths can qualitatively help to assess the voltage loss due to absorber crystalline quality. The higher β_{112}, the lower the crystalline quality, and the higher could be the associated voltage loss. From Figure 4c, it is evident that β_{112} has higher values at the absorber surfaces (lower grazing angles) and decreases toward the bulk (higher grazing angles). In the bulk of the absorbers, at each respective deposition temperature as shown in Figure 4c, Ag incorporation reduces β_{112} establishing the beneficial effect of Ag incorporation in improving the crystalline quality. Ga and In exhibit limited interdiffusion for lower deposition temperatures; crystallizing in different chalcopyrite phases across the absorber thickness. Though the absorbers have different compositional gradients showing the possibility of several chalcopyrite phases across their thickness, mainly two kinds of phases exist (Figure 4d). At the respective depth from the absorber surface, the diffractograms of higher grazing angles (5°) suggest a dominating primary phase where the Ga percentage is lower, which is denoted as 112-Primary (Figure 4d) and the other chalcopyrite is the Ga-rich phase denoted as 112_Ga rich (Figure 4d). Furthermore, when the absorber growth dynamics is limited by the deposition temperature (i.e., for low deposition temperature), the presence of Ag improved the Ga interdiffusion, incorporating a higher amount of Ga into the chalcopyrite primary phase. We could draw this conclusion by observing the relative intensity of the 112-Primary peak compared to the 112_Ga-rich peak, which is high for Ag-containing absorbers (Figure 4d) compared to Ag-free absorbers shown in Figure S5c, Supporting Information. Due to a relatively high interdiffusion for 530 °C absorbers, which helps in establishing a continuous Ga gradient, the distinct secondary Ga-rich phase is not evident toward their surface.

Figure 5a–l shows the top and cross-sectional view of scanning electron microscope (SEM) images of stage-3 ACIGSe absorbers (AAC, 0% and 2%), which were deposited at 530, 450, and 370 °C. Both top view and cross-sectional images show a larger grain size

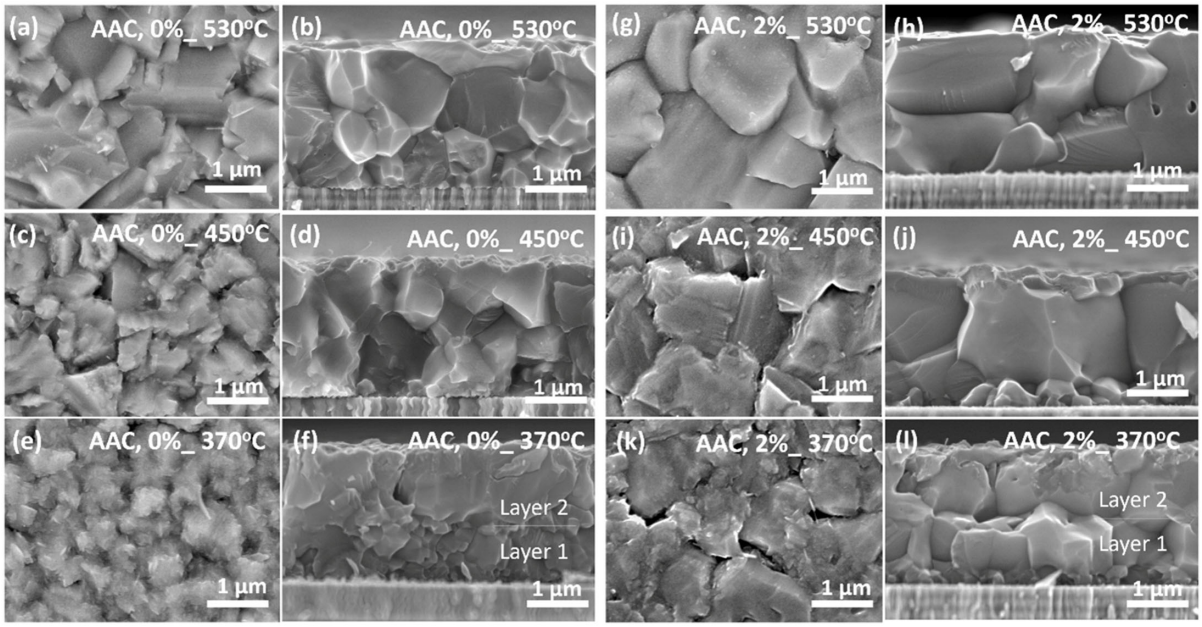

Figure 5. SEM images of ACIGSe films showing the top view a,c,e,g,i,k) and cross-sectional view b,d,f,h,j,l) at the end of stage-3. The deposition temperature and AAC are (a,b) 530 °C and AAC, 0%, (g,h) 530 °C and AAC, 2%, (c,d) 450 °C and AAC, 0%, (i,j) 450 °C and AAC, 2%, (e,f) 370 °C and AAC, 0%, (k,l) 370 °C and AAC, 2%.

for Ag-containing absorbers at all deposition temperatures compared to the Ag-free samples. Especially at a low deposition temperature of 370 °C, the grain growth of Ag-free samples (AAC, 0%) is severely limited showing smaller grains and the film morphology is distinguishable as a two-layer structure (Figure 5f). These SEM images reveal that for the absorber deposition at low temperatures, the incorporation of Ag helps in achieving large grain size (Figure 5j,l). In chalcopyrite devices, the grain boundaries in the absorbers with a high defect density can potentially induce voltage losses.[37] Smaller grains have a larger grain boundary area and thus can potentially cause a greater voltage loss. For the absorbers of AAC 0%, compared to the larger grains (Figure 5b) produced at high temperature, the smaller grains of the absorbers produced at low temperatures (Figure 5d,f) contribute to noticeable voltage losses (as shown in Table 1).

2.6. V_{OC} Loss Contributions from Bandgap and Nonradiative Losses at the Absorber Level

The use of absolute PL measurements on the solar absorber determining the V_{OC} losses has been explored predicting the efficiency of a solar cell.[38–40] For an ideal direct-bandgap semiconductor with zero density of states in the bandgap region, the PL emission appears at $E_g + k_B T/2$, (k_B, Boltzmann constant; T, absolute temperature) revealing the bandgap.[39] For an ideal solar cell with an absorber of bandgap E_g, governed by the detailed balance limit (Shockley–Queisser (SQ limit)), the device can exhibit the maximum possible open-circuit voltage of V_{OC}^{SQ} (SQ limit). For a given bandgap one can find the V_{OC}^{SQ} values and its detailed calculation reported elsewhere.[41,42] In this SQ limit case, for the ideal solar cell device, the absorber is assumed to have a step function-like absorptance spectrum referring to V_{OC}^{SQ}. However, in practical cases, the absorptance spectra of an absorber rather show a broadening of the absorption edge due to the presence of sub-bandgap absorption, a bandgap gradient, and bandgap fluctuations that all contribute to this broadening effect.[43] As a result of the broadening, the PL peak shifts to energies lower than the actual bandgap energy.[44] For a simple approximation, we can use this PL peak maximum to determine this reduced bandgap, called radiative bandgap ($E_{g\text{-}PL}$). Using this reduced radiative bandgap the maximum achievable reduced radiative limit voltage can be calculated, here in **Figure 6**a it is designated as $\left(V_{OC}^{SQ}\right)_{PL}$.[43,45] Since the PL emission typically occurs at lower energies than the bandgap, we can assume that the radiative losses are already accounted for due to this shift in the PL peak maximum when considering the radiative bandgap, $E_{g\text{-}PL}$. In the real photovoltaic device, the NR recombination, for example, at the grain boundaries, interfaces, or defects can further decrease the V_{OC}. These NR losses (NR losses) exclusively originating from the absorber can be determined by recording the PL quantum yield (PLQY) and then calculated as $k_B T \ln(\text{PLQY})$. The quasi-Fermi-level splitting (QFLS) of the absorber can be estimated as the $\left(V_{OC}^{SQ}\right)_{PL}$ minus the NR losses. Beyond the absorber-level voltage losses, the additional voltage losses across the interfaces can be calculated as QFLS/q (where q is elementary charge), minus the device V_{OC}.[46] All these values of various voltage losses are presented in Table 1 for selected ACIGSe devices.

From Table 1, the QFLS values of the ACIGSe (AAC, 2%) are found to be higher than their Ag-free compositions (AAC, 0%) at the respective absorber deposition temperature. This could be

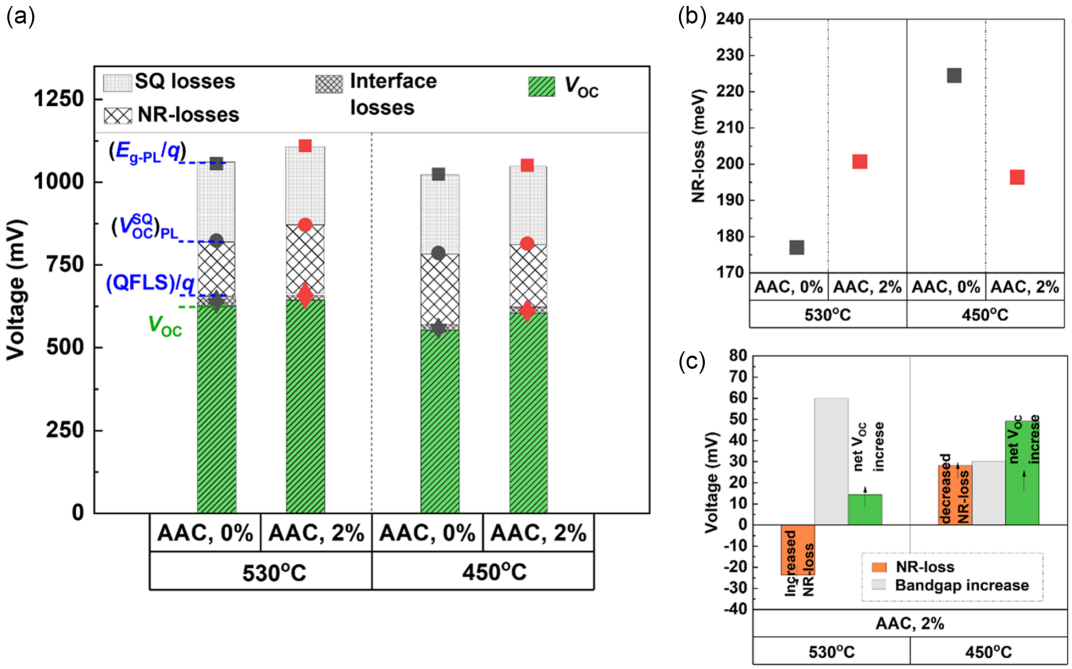

Figure 6. a–c) Origin of voltage losses for the solar cell devices containing ACIGSe absorbers of AAC, 0% and 2% deposited at 530 and 450 °C: (a) a schematic presenting the V_{OC} loss contributions from various types of losses, (b) magnitude of NR losses, and (c) the changes in bandgap and NR losses of AAC, 2% devices relative to AAC, 0% at their respective deposition temperature, and their contributions for the net increment in the device V_{OC} (contributions shown here are excluded from interface losses).

due to a higher bandgap for Ag-containing absorbers. We already anticipated a higher bandgap for Ag-containing absorbers from the GDOES depth profiles earlier. This anticipation was found to be true on determining the bandgap from the PL measurements, the absorbers containing Ag (AAC, 2%) showed higher bandgaps ($E_{g\text{-}PL}$) compared to the Ag-free absorbers of AAC, 0% at their respective deposition temperature. An increased bandgap for ACIGSe (AAC, 2%) also sets an increased $\left(V_{OC}^{SQ}\right)_{PL}$ (Figure 6a and Table 1) and hence an increased device V_{OC}. However, for Ag-containing absorbers an equivalent magnitude of bandgap increase is not reflected in the device's V_{OC}. The NR losses and interfacial recombinations in the devices seem to affect the final V_{OC}. The NR loss contribution arising from the absorbers is shown in Figure 6b. For the high-temperature process at 530 °C, the Ag-containing samples (AAC, 2%) show higher NR loss compared to pure CIGSe (AAC, 0%). At low absorber deposition temperatures, 450 °C, the NR loss is relatively lower for Ag-containing absorbers (AAC, 2%) compared to pure CIGSe (AAC, 0%). However, the overall magnitude of NR losses is determined to be increased as the deposition temperature of the absorber reduced (Figure 6b). For these low-temperature Ag-containing absorbers the increased grain size with less structural imperfections helps to yield low NR losses over Ag-free compositions. However, between them, the V_{OC} loss contribution originating from interface losses is found to be minimal.

Figure 6c schematically provides information on the magnitude of the net increase in device V_{OC} for Ag-containing devices with respect to Ag-free compositions at their respective deposition temperature. For ACIGSe (AAC, 2%) absorbers of 530 °C, the net increments in the device V_{OC} display the contribution from an increased bandgap partially reduced by high NR losses (negative scale). Whereas, for the ACIGSe (AAC, 2%) absorbers of 450 °C, the net increment in the device V_{OC} consists of the added contributions from a moderately increased bandgap and the reduced NR losses (positive scale). In summary, the improvement in V_{OC} in the Ag-containing low-temperature-processed devices can be attributed to two main factors: first, an increase in bandgap energy predominantly due to improved Ga interdiffusion that leads to higher V_{OC} values and second, the passivation of NR recombination centers, reducing the relative voltage loss.

3. Conclusion

In this study, it is shown that a minimal amount of Ag incorporation—about 0.5–1.4 at% in CIGSe—significantly influences the structural and microstructural characteristics and hence the crystalline quality of the resulting ACIGSe solar absorbers. The Ag incorporation is beneficial for the low-temperature absorber deposition, as its presence improves the crystalline quality by increasing elemental interdiffusion and grain growth. The smallest amount of Ag—as low as 0.5 at%—considered in this study is proven to be effective in improving the device's V_{OC} especially for the absorbers deposited at low temperature. Ag incorporation significantly broadens the process window for high-quality ACIGSe absorbers and enables lower deposition temperatures, providing greater versatility for

adapting substrates with low thermal stability. A Cu-deficient crystal lattice, characterized by a low CGI (<0.86), promotes incorporation of higher amounts of Ag into the bulk of the absorber in chalcopyrite form; however—using three-stage thermal coevaporation for absorber deposition—its uniform distribution across the absorber bulk depends on the specific Cu content (CGI). In the absorber's bulk, when Cu surplus is available, Cu is preferred over Ag to form a chalcopyrite structure. The presence of Ag influences the Ga and In distribution profiles and in effect increases the absorber bandgap. Following our deposition process, the optimal overall absorber ACGI was found to be around 0.86–0.88 (where the CGI is 0.84–0.86) with an AAC of 2% (0.5 at%). Within this AAC range, our ACIGSe absorbers yield a best device PCE of 18.2%. With the Ag incorporation into the absorbers, the net increment in the device V_{OC} is affected by the bandgap increase and the NR losses. For the absorbers produced at low deposition temperature, the presence of Ag was proven to be effective in reducing those NR losses relative to the Ag-free composition, yielding a relatively high QFLS and hence a relatively high device V_{OC}. The current results produced in understanding the Ag influence on the low-temperature-deposited low-bandgap ACIGSe absorbers yielding high V_{OC} will help expand substrate options and enhance solar cell design flexibility. This advancement could aid in designing monolithic integration of low-bandgap ACIGSe solar cells into tandem structures, pairing them with wide-bandgap, high-temperature-processable Ga-rich chalcopyrites in, for example, superstrate configuration. Such a design could create entirely chalcopyrite-based monolithic tandem solar cells, paving the way for more efficient and versatile solar cell technologies.

4. Experimental Section

Fabrication of ACIGSe Devices: SLG substrates were coated with 800 nm Mo metal by direct current sputtering. On these Mo/SLG substrates, ACIGSe (AAC, 0%, 2%, 3%, and 6%) absorbers were deposited as described in the main text. Before the deposition of the buffer layer, the absorbers were rinsed with aqueous NH_3 (1 mol L^{-1}). A 50 nm cadmium sulfide (CdS) buffer layer was grown on these absorbers by chemical bath deposition. For the CdS deposition, the solution was prepared by adding cadmium acetate (2.5 mM, 98% purity), thiourea (0.05 M, >99% purity), aqueous ammonia solution (maximum contamination ≤260 ppm, grade: GPR Rectapure) into the deionized water and the resulting solution was heated to 60 °C while stirring. The ACIGSe (AAC, 0%, 2%, 3%, and 6%) substrates were dipped into this stirring solution during heat-up (60 °C) for 16–18 min to obtain the CdS layer. On top of this buffer layer, a window layer stack comprising intrinsic zinc oxide (40 nm) and aluminum-doped zinc oxide (150 nm) was deposited by radio frequency sputtering. Metallization for the front contact grid was done by evaporating a stack of nickel/aluminum/nickel (25 nm/3 µm/25 nm) using e-beam evaporation and appropriate shadow masks.

Absorber Characterization: ACIGSe elemental compositions in at% were obtained by XRF analysis using the instrument Rigaku WD-XRF ZSX Primus II. The elemental depth profile on CIGSe/ACIGSe absorbers was obtained using GDOES on a Spectruma GDA 650 instrument. The GIXRD measurements were carried out with help of the PANalytical X'Pert Pro MPD X-ray diffractometer employing the Cu K-alpha wavelength. SEM top and cross-sectional images were recorded using the SEM JSM-7610F-FE-SEM equipped with in-lens secondary electron / backscattered electron detectors.

The PL measurements were carried out using a red diode laser with a wavelength of 637 nm and beam diameter of 2.6 mm. The calibration process involved both intensity and spectral calibration. The intensity of the laser light was calibrated to 1 sun incident photon flux density. Moreover, the PL spectrum was corrected using a halogen lamp. The PL emission signal was collected using two off-axis parabolic mirrors and subsequently was directed through an optical fiber into the spectrometer, where it was detected by an InGaAs array. The samples showed interference fringes. To remove the effect of interference and determine the PL peak position (Figure S6, Supporting Information), the samples were covered with polystyrene spheres, (See Supporting Information and ref [s1–s3]). Further details on the method of PL measurement can be found in the supporting information and in previous reports.[39,40,47]

Absorber Characterization: Solar Cell Characterization: The current–voltage measurements were conducted on 0.91 cm^2 active area cells using a WACOM A+ solar simulator (1000 W m^{-2}) under standard conditions at 25 °C. For these devices, EQE measurements were carried out at HZB using an in-house-built setup recording the spectral response from 300 to 1400 nm wavelength with a step size of 10 nm. For the smaller-area cells, the current–voltage measurements were carried out at the University of Luxembourg, using a standard solar simulator under one sun illumination (1000 W m^{-2}). The solar cell active areas were determined through a microscope.

Supporting Information

Supporting Information is available from the Wiley Online Library or from the author.

Acknowledgements

The authors acknowledge B. Bunn, T. Münchenberg, K. Mayer-Stillrich, M. Hartig, N. El-Ganainy, F. Mai, K.S. Mohammad, B. Belkin for technical support in device fabrication and characterization. The authors thank Dr. Reiner Klenk for providing feedback on the discussion of the results. The authors also thank Prof. Susanne Siebentritt from University of Luxembourg for providing the facilities for photoluminescence measurement and solar cell device fabrication and measurements. S.P. and I.L. acknowledge the Horizon Europe Framework Programme (HORIZON), Marie Skłodowska-Curie Actions postdoctoral Fellowships 2021 (HORIZON-MSCA-2021-PF-01), project name: FaWBChaLT, project number: 101065174. Further, S.P. and I.L. thank Andreas Zimmermann from the company Sunplugged for the collaboration and funding acquisition. SG acknowledges Luxembourgish Fonds National de la Recherche (FNR) and the grant number C20/MS/14735144/TAILS.

Conflict of Interest

The authors declare no conflict of interest.

Author Contributions

Sateesh Prathapani: conceptualization (lead); formal analysis (lead); funding acquisition (lead); investigation (lead); methodology (lead); project administration (lead); writing—original draft (lead). **Sevan Gharabeiki**: investigation (supporting); methodology (supporting); writing—review & editing (supporting). **Jakob Lauche**: resources (supporting). **René Schwiddessen**: conceptualization (supporting); methodology (supporting); resources (supporting); writing—review & editing (supporting). **Pablo Reyes-Figueroa**: methodology (supporting); validation (supporting); writing—review & editing (supporting). **Nikolaus Weinberger**: investigation (supporting); resources (supporting); writing—review & editing (supporting). **Michele Melchiorre**: investigation (supporting); resources (supporting); validation (supporting). **Rutger Schlatmann**: resources (supporting). **Iver Lauermann**: funding acquisition (supporting); methodology (supporting); resources (supporting); supervision (supporting);

writing—review & editing (supporting). **Christian Alexander Kaufmann**: methodology (supporting); resources (supporting); supervision (supporting); validation (supporting); writing—review & editing (supporting).

Data Availability Statement

The data that support the findings of this study are available in the supplementary material of this article.

Keywords

ACIGSe, Ag-based chalcopyrite solar cells, $(Ag,Cu)(In,Ga)Se_2$, nonradiative voltage losses, open-circuit voltage losses

Received: December 5, 2024
Revised: January 18, 2025
Published online: January 31, 2025

[1] H. Liang, J. Feng, D. Carlos, M. Krause, X. Wang, R. Ezra Alvianto, *Joule* **2023**, *7*, 2859.
[2] M. Jošt, E. Köhnen, A. Al-Ashouri, T. Bertram, Š. Tomšič, A. Magomedov, E. Kasparavicius, T. Kodalle, B. Lipovšek, V. Getautis, R. Schlatmann, C. A. Kaufmann, S. Albrecht, M. Topič, *ACS Energy Lett.* **2022**, *7*, 1298.
[3] X. Liu, J. Zhang, L. Tang, J. Gong, W. Li, Z. Ma, Z. Tu, Y. Li, R. Li, X. Hu, C. Shen, H. Wang, Z. Wang, Q. Lin, G. Fang, S. Wang, C. Liu, Z. Zhang, J. Li, X. Xiao, *Energy Environ. Sci.* **2023**, *16*, 5029.
[4] K. Makita, Y. Kamikawa, T. Koida, H. Mizuno, R. Oshima, Y. Shoji, S. Ishizuka, T. Takamoto, T. Sugaya, *Prog. Photovoltaics Res. Appl.* **2023**, *31*, 71.
[5] R. Verduci, V. Romano, G. Brunetti, N. Yaghoobi Nia, A. Di Carlo, G. D'Angelo, C. Ciminelli, *Adv. Energy Mater.* **2022**, *12*, 2200125.
[6] M. Krause, S. C. Yang, S. Moser, S. Nishiwaki, A. N. Tiwari, R. Carron, *Sol. RRL* **2023**, *7*, 2201122.
[7] K. Zajac, S. Brunner, C. A. Kaufmann, R. Caballero, H.-W. Schock, A. Rahm, C. Scheit, H. Zachmann, F. Kessler, R. Wuerz, P. Schulke, in *35th IEEE Photovoltaic Specialists Conference*, Honolulu, HI, USA **2010**, P. 000016.
[8] T. Feurer, P. Reinhard, E. Avancini, B. Bissig, J. Löckinger, P. Fuchs, R. Carron, T. P. Weiss, J. Perrenoud, S. Stutterheim, S. Buecheler, A. N. Tiwari, *Prog. Photovoltaics Res. Appl.* **2017**, *25*, 645.
[9] J. Haarstrich, H. Metzner, M. Oertel, C. Ronning, T. Rissom, C. A. Kaufmann, T. Unold, H. W. Schock, J. Windeln, W. Mannstadt, E. Rudigier-Voigt, *Sol. Energy Mater. Sol. Cells* **2011**, *95*, 1028.
[10] R. Carron, S. Nishiwaki, T. Feurer, R. Hertwig, E. Avancini, J. Löckinger, S. C. Yang, S. Buecheler, A. N. Tiwari, *Adv. Energy Mater.* **2019**, *9*, 1900408.
[11] S. C. Yang, J. Sastre, M. Krause, X. Sun, R. Hertwig, M. Ochoa, A. N. Tiwari, R. Carron, *Sol. RRL* **2021**, *5*, 2100108.
[12] D. Kim, S. S. Shin, S. M. Lee, J. S. Cho, J. H. Yun, H. S. Lee, J. H. Park, *Adv. Funct. Mater.* **2020**, *30*, 2001775.
[13] S. Y. Kim, H. Yoo, T. R. Rana, T. Enkhbat, G. Han, J. H. Kim, S. Song, K. Kim, J. Gwak, Y. J. Eo, J. H. Yun, *Adv. Energy Mater.* **2018**, *8*, 1801501.
[14] J. Keller, K. V. Sopiha, O. Stolt, L. Stolt, C. Persson, J. J. S. Scragg, T. Törndahl, M. Edoff, *Prog. Photovoltaics Res. Appl.* **2020**, *28*, 237.
[15] S. Prathapani, Y. Zhan, *Energy Technol.* **2021**, *9*, 2100193.
[16] J. Keller, L. Stolt, T. Törndahl, M. Edoff, *Sol. RRL* **2023**, *7*, 2300208.
[17] A. J. M. Prot, M. Melchiorre, F. Dingwell, A. Zelenina, H. Elanzeery, A. Lomuscio, T. Dalibor, M. Guc, R. Fonoll-Rubio, V. Izquierdo-Roca, G. Kusch, R. A. Oliver, S. Siebentritt, *APL Mater.* **2023**, *11*, 101120.
[18] M. Edoff, T. Jarmar, N. S. Nilsson, E. Wallin, D. Högström, O. Stolt, O. Lundberg, W. Shafarman, L. Stolt, *IEEE J. Photovolt.* **2017**, vol. *7*, p. 1789.
[19] L. H. Tu, N. T. T. Tran, S. K. Lin, C. H. Lai, *Adv. Energy Mater.* **2023**, *13*, 2301227.
[20] J. Keller, K. Kiselman, O. Donzel-Gargand, N. M. Martin, M. Babucci, O. Lundberg, E. Wallin, L. Stolt, M. Edoff, *Nat. Energy* **2024**, *9*, 467.
[21] S. C. Yang, T. Y. Lin, M. Ochoa, H. Lai, R. Kothandaraman, F. Fu, A. N. Tiwari, R. Carron, *Nat. Energy* **2023**, *8*, 40.
[22] K. V. Sopiha, J. K. Larsen, O. Donzel-Gargand, F. Khavari, J. Keller, M. Edoff, C. Platzer-Björkman, C. Persson, J. J. S. Scragg, *J. Mater. Chem. A* **2020**, *8*, 8740.
[23] K. Kim, J. W. Park, J. S. Yoo, J. S. Cho, H. D. Lee, J. H. Yun, *Sol. Energy Mater. Sol. Cells* **2016**, *146*, 114.
[24] S. Siebentritt, L. Gütay, D. Regesch, Y. Aida, V. Deprédurand, *Sol. Energy Mater. Sol. Cells* **2013**, *119*, 18.
[25] H. Wilhelm, H.-W. Schock, R. Scheer, *J. Appl. Phys.* **2011**, *109*, 084514.
[26] M. Sood, A. Urbaniak, C. Kameni Boumenou, T. P. Weiss, H. Elanzeery, F. Babbe, F. Werner, M. Melchiorre, S. Siebentritt, *Prog. Photovoltaics Res. Appl.* **2022**, *30*, 263.
[27] T. Kodalle, M. D. Heinemann, D. Greiner, H. A. Yetkin, M. Klupsch, C. Li, P. A. van Aken, I. Lauermann, R. Schlatmann, C. A. Kaufmann, *Sol. RRL* **2018**, *2*, 1800156.
[28] K. Sakurai, T. Neumann, R. Hesse, D. Abou-Ras, P. Jablonski, A. Neisser, C. Kaufmann, S. Niki, R. Scheer, H.-W. Schock, *Thin Solid Films* **2007**, *515*, 6222.
[29] C. A. Kaufmann, R. Caballero, T. Unold, R. Hesse, R. Klenk, S. Schorr, M. Nichterwitz, H.-W. Schock, *Sol. Energy Mater. Sol. Cells* **2009**, *93*, 859.
[30] T.-P. Hsieh, C.-C. Chuang, C.-S. Wu, J.-C. Chang, J.-W. Guo, W.-C. Chen, *Solid State Electron.* **2011**, *56*, 175.
[31] R. Mainz, E. Simsek Sanli, H. Stange, D. Azulay, S. Brunken, D. Greiner, S. Hajaj, M. D. Heinemann, C. A. Kaufmann, M. Klaus, Q. M. Ramasse, H. Rodriguez-Alvarez, A. Weber, I. Balberg, O. Millo, P. A. Van Aken, D. Abou-Ras, *Energy Environ. Sci.* **2016**, *9*, 1818.
[32] M. Latha, R. Aruna-Devi, S. Velumani, J. Santoyo-Salazar, F. de Moure-Flores, *Adv. Powder Technol.* **2019**, *30*, 2980.
[33] J. Lin, G. Song, Y. Chen, F. Hu, Y. Wu, J. You, *J. Solid State Chem.* **2024**, *331*, 124507.
[34] B. D. Cullity, S. R. Stock, Elements of X-Ray diffraction **2014**, p.403, Pearson.
[35] I. M. Kötschau, H. W. Schock, *J. Appl. Crystallogr.* **2006**, *39*, 683.
[36] J. Dietrich, D. Abou-Ras, T. Rissom, T. Unold, H. W. Schock, C. Boit, *Conf. Rec. IEEE Photovoltaic Specialists Conference*. Seattle, WA, USA **2011**, p. 000343.
[37] S. Siebentritt, *Sol. Energy Mater. Sol. Cells* **2011**, *95*, 1471.
[38] S. Shukla, M. Sood, D. Adeleye, S. Peedle, G. Kusch, D. Dahliah, M. Melchiorre, G. M. Rignanese, G. Hautier, R. Oliver, S. Siebentritt, *Joule* **2021**, *5*, 1816.
[39] S. Siebentritt, T. P. Weiss, M. Sood, M. H. Wolter, A. Lomuscio, O. Ramirez, *J. Phys Mater.* **2021**, *4*, 042010.
[40] M. H. Wolter, R. Carron, E. Avancini, B. Bissig, T. P. Weiss, S. Nishiwaki, T. Feurer, S. Buecheler, P. Jackson, W. Witte, S. Siebentritt, *Prog. Photovoltaics Res. Appl.* **2022**, *30*, 702.
[41] W. Shockley, H. J. Queisser, *J. Appl. Phys.* **1961**, *32*, 510.
[42] S. Rühle, *Sol. Energy* **2016**, *130*, 139.

[43] S. Siebentritt, U. Rau, S. Gharabeiki, T. P. Weiss, A. Prot, T. Wang, D. Adeleye, M. Drahem, A. Singh, *Faraday Discuss.* **2022**, *239*, 112.
[44] D. Abou-Ras, *J. Vac. Sci. Technol. A* **2024**, *42*, 022803.
[45] J. Mattheis, U. Rau, J. H. Werner, *J. Appl. Phys.* **2007**, *101*, 113519.
[46] M. Sood, J. Bombsch, A. Lomuscio, S. Shukla, C. Hartmann, J. Frisch, W. Bremsteller, S. Ueda, R. G. Wilks, M. Bär, S. Siebentritt, *ACS Appl. Mater. Interfaces* **2022**, *14*, 9676.
[47] S. Gharabeiki, M. U. Farooq, T. Wang, M. Sood, M. Melchiorre, C. Kaufmann, A. Redinger, S. Siebentritt, *J. Phys. Energy* **2024**, *6*, 035008.